Shadow imaging of geostationary satellites: experimental demonstration with accurate polychromatic modelling of diffraction and atmospheric disturbances

Hanae Labriji, Olivier Herscovici-Schiller, Frédéric Cassaing

▶ **To cite this version:**

Hanae Labriji, Olivier Herscovici-Schiller, Frédéric Cassaing. Shadow imaging of geostationary satellites: experimental demonstration with accurate polychromatic modelling of diffraction and atmospheric disturbances. Advanced Maui Optical and Space Surveillance Technologies Conference (AMOS), Sep 2022, MAUI, United States. hal-03882891

HAL Id: hal-03882891
https://hal.science/hal-03882891

Submitted on 2 Dec 2022

HAL is a multi-disciplinary open access archive for the deposit and dissemination of scientific research documents, whether they are published or not. The documents may come from teaching and research institutions in France or abroad, or from public or private research centers.

L'archive ouverte pluridisciplinaire **HAL**, est destinée au dépôt et à la diffusion de documents scientifiques de niveau recherche, publiés ou non, émanant des établissements d'enseignement et de recherche français ou étrangers, des laboratoires publics ou privés.

Shadow imaging of geostationary satellites: experimental demonstration with accurate polychromatic modelling of diffraction and atmospheric disturbances

Hanae Labriji, Olivier Herscovici-Schiller & Frédéric Cassaing
DTIS, ONERA, Université Paris Saclay, F-91123 Palaiseau - France

ABSTRACT

Shadow imaging is an original and simple method to meet the challenge of characterizing and identifying distant satellites. It is based on observing the shadow cast on the ground during a stellar occultation. The shadow is sampled, then the signal is processed in order to derive the contour of the object. Our objective is to identify and quantify the limitations of the method and to optimize and demonstrate solutions.

We show that atmospheric refraction and turbulence can be numerically corrected and that Fresnel diffraction can be efficiently modelled using the decomposition of the incident light in a truncated basis of Hermite-Gauss functions. This leads to sampling requirements for the shadow in terms of spectral width, position and number of telescopes for a given specification of resolution and maximum size of the satellite. For instance, submetrically resolving a 15 m object at 40 000 km from the ground necessitates a spectral bandwidth of 40 nm. Moreover, the shadow should be traced over about 60 m and a good sampling in this case demands a telescope to be placed almost every 30 cm.

Our inversion algorithm, based on a *maximum a posteriori* estimator coupled with non-linear modern optimization, confirms from simulation and small-scale laboratory data that successful reconstructions can be performed with stars of magnitude 6.

An innovative output of this work is that the wide and continuous spectrum of the stars can be used to relax requirements on the spatial sampling of the shadow.

1. INTRODUCTION

Resolved imaging of geostationary satellites is a high challenge in space surveillance. To the best of our knowledge, there is no proven effective method for ground-based imaging of geosynchronous satellites at sub-metric resolution. Decametric telescopes are too small [1], Extremely Large Telescopes are in construction, and coherent telescope arrays have mainly demonstrated fringe acquisition in fortunate good conditions with decametric baselines [2].

Shadow imaging is a method that allows to retrieve the geometric contour of asteroids when occulting a star [3]. It was first proposed to provide submetric resolution on geostationary satellites with a low-cost hardware by R. Burns and colleagues in 2005 [4]. Since then, D. M. Douglas [5] studied light propagation and inversion using the Gerchberg and Saxton algorithm for different observing configurations. After investigating the inversion of numerically generated data [6], R. Paxman set up an experiment reproducing the effect of diffraction on a small scale [7], and proved that it is possible to recover sub-metric details on real data, in very comfortable photometric conditions. But the chromaticity of light propagation requires the detection in narrow spectral channels [8].

Since we are convinced that shadow imaging is a powerful and efficient technique, our approach is to analyze in details both the physics of light propagation from the satellite to the detector and the processing of the acquired data. Identifying and optimizing the free parameters, validating our results in laboratory, are necessary steps to define a future system and evaluate its performance. After the investigation of atmospheric disturbances such as chromatic refraction [9] and scintillation [10], we concentrate here on chromatic effects to maximize the sensitivity using a large spectral bandpass.

In section 2, we first recall the principle of shadow imaging and describe the direct model that we use to account for propagation. Then, in section 3, we derive the sampling parameters, describe the inversion algorithm supported by simulation results. Next, in section 4, we describe our experimental setup and show the reconstructions using our inversion algorithm for various polychromatic configurations.

2. A DIRECT MODEL FOR SHADOW IMAGING PROPAGATION

2.1 Principle of the method

The basic concept of shadow imaging of geostationary satellites is described in Fig. 1. When the satellite occults a star, its shadow is cast on the ground. Due to the relative motions, the shadow moves from west to east at a speed between 2700 m/s and 3500 m/s, depending on the longitude and the latitude of both the satellite and the observer. This motion can be used to reduce the number of sub-pupils since the 2-dimensional shadow can be digitally acquired using a single row of small telescopes placed perpendicular to the predicted trajectory of the shadow. Thus, at each moment of the occultation, a column of the 2D shadow is recorded. Each telescope acts as a light collecting bucket, delivering the value of one pixel per column. A small focal-plane detector is used to exclude contributions from other directions than the target star. Layering all the acquired lines together reveals the complete 2D satellite shadowgram. The sampling frequency must be larger than 1 kHz since the typical width of the core of a diffraction structure – the Fresnel scale $\sqrt{\lambda z_{\mathrm{GEO}}/2}$ – is around 3 m for a wavelength λ around 0.5 µm and a satellite distance from the observer z_{GEO} close to 40 000 km [3]. To optimize performance, the weak but large-band flux from the star is spectrally dispersed over several pixels. These small channels shadowgrams are then processed numerically to recover the satellite contour.

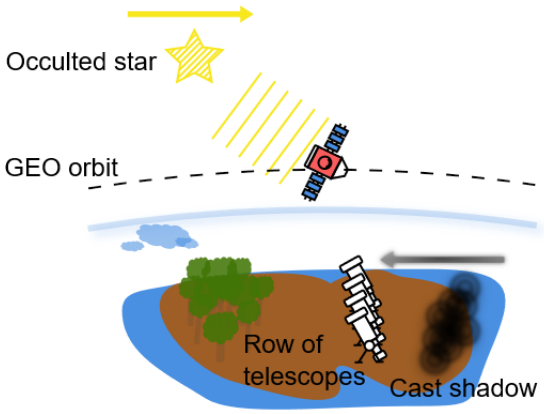

Fig. 1: Diffraction by an occulting satellite.

This shadow imaging setup is nothing but Gabor holography. Each telescope performs the homodyne detection of the diffracted wave, using the plane wave from the star as a local oscillator (LO), which provides a phase reference for the coherent detection all across the hectometric pupil and allow to numerically combine the sampled intensities rather than the optical coherent beams, as with large telescopes or interferometers. The main drawback is the need to find a sufficiently bright star aligned with the targets, which calls for movable telescopes accurately positioned [4].

2.2 A direct model for shadow imaging

As illustrated in Fig. 1, the shadow is not the perfect geometric contour of the satellite, it is altered by the diffraction rings resulting from the shadow propagation. It is then necessary to solve an inverse problem based on a very fine knowledge of the complete chain of light propagation. In addition, along its path through the Earth's atmosphere, the light beams undergo refraction and turbulence.

2.2.1 Fresnel propagation

The major physical phenomenon involved is the diffraction of light. Within the framework of the paraxial approximation, the amplitude U_z of a wave U_0 propagated to a distance z is given by [11]:

$$U_z(x,y) = \frac{\exp(\mathrm{i}kz)}{\mathrm{i}\lambda z} \iint_{-\infty}^{\infty} U_0(X,Y) \exp\left[\mathrm{i}\frac{k}{2z}\left((X-x)^2+(Y-y)^2\right)\right] \mathrm{d}X\mathrm{d}Y, \tag{1}$$

where λ is the observation wavelength, $k = 2\pi/\lambda$ is the wave number and $\mathrm{i}^2 = -1$. And as depicted in Fig. 2, (X,Y) and (x,y) are, respectively, the coordinates at the satellite plane and at the observer plane and z is the coordinate on

the optical axis star-satellite-observer, i.e. z equals zero on the satellite plane and z_{GEO} at the observer plane. The dimensionless number that characterizes diffraction by an object of size T is the Fresnel number, given by:

$$N_F = \frac{T^2}{\lambda z}. \tag{2}$$

This number varies between 5 and 100 for geostationary satellites oberved in the visible from the ground.

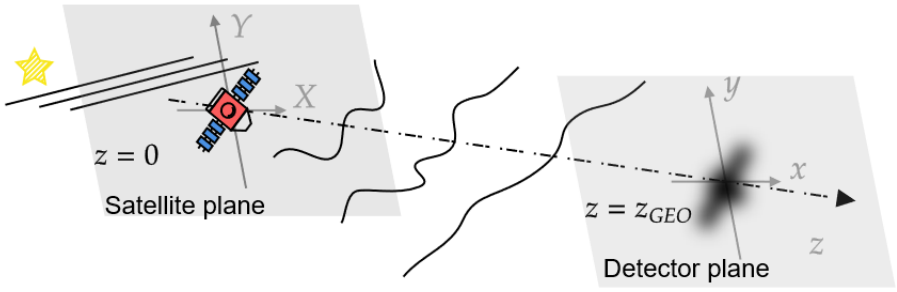

Fig. 2: Notations for diffraction.

In the case of satellite shadow imaging, the incident wave is considered to be plane and the function U_0 simply represents the transmittance of the object. To avoid infinite integration bounds, we reduce the problem to the study of the propagation of the object's absorbance $\overline{U_0} := 1 - U_0$ by applying the Babinet principle [12]. Injecting in Eq. (1):

$$\begin{aligned} U_z(x,y) = &\frac{\exp(\mathrm{i}kz)}{\mathrm{i}\lambda z} \iint_{-\infty}^{\infty} \exp\left[\mathrm{i}\frac{k}{2z}\left((X-x)^2+(Y-y)^2\right)\right] \mathrm{d}X\mathrm{d}Y \\ &- \frac{\exp(\mathrm{i}kz)}{\mathrm{i}\lambda z} \iint_{-T/2}^{T/2} \overline{U_0}(X,Y) \exp\left[\mathrm{i}\frac{k}{2z}\left((X-x)^2+(Y-y)^2\right)\right] \mathrm{d}X\mathrm{d}Y. \end{aligned} \tag{3}$$

The first integral in Eq. (3) gives the propagation of a plane wave up to a distance z, which remains a plane wave, while the second integral is more complicated to derive as it does not have any analytical solution. Various methods exist to compute numerically this second integral [11]. The two most recommended ones in the literature are based on Fourier transforms, either by convolving the object with the chirp function [13], or by computing directly the Fourier Transform ($\mathbb{FT}$) of the object multiplied by the chirp, noticing that Eq. (1) can be written:

$$U_z(x,y) = \frac{\exp(\mathrm{i}kz)}{\mathrm{i}\lambda z} \exp\left[\mathrm{i}\frac{\pi}{\lambda z}\left(x^2+y^2\right)\right] \mathbb{FT}\left\{(X,Y) \mapsto U_0(X,Y) \exp\left[\mathrm{i}\frac{\pi}{\lambda z}\left(X^2+Y^2\right)\right]\right\}\left(\frac{x}{\lambda z}, \frac{y}{\lambda z}\right). \tag{4}$$

These methods have the advantage of being fast to compute thanks to the Fast Fourier Transform algorithm, but present several non-physical constraints on the discretization of the field on the object and image plane [14, 15, 16]. In addition, they do not provide any significant information on the geometric extent of the shadow, a major parameter in the dimensioning of the shadow imaging system.

We have thus chosen to adopt a method that is less popular in the literature, yet offering a physical background that facilitates the understanding of the phenomenon. It consists in using the Hermite-Gauss (HG) functions, which both form an orthonormal basis of integrable square functions and are solution of the wave equation in the paraxial approximation [17]. The calculation of the diffractogram generated by an object is simply based on the decomposition of the object in this basis of functions [18]. HG functions, denoted by ψ_n (where n is a natural number) propagate analytically following:

$$\psi_n(x,z,W(z),R(z)) = \frac{H_n(\sqrt{2}x/W)}{\sqrt{2^{n+1/2}n!\sqrt{\pi}W}} \exp\left(-\frac{x^2}{W^2}\right) \exp\left[-jk\frac{x^2}{2R} + j\phi_n(W,R)\right], \tag{5}$$

where H_n is the Hermite polynomial of order n, $W(z)$ is the waist, $R(z)$ is the phase front radius of curvature and ϕ_n is known as the Gouy phase, given by:

$$W^2(z) = W_0^2\left[1+\left(\frac{\lambda z}{\pi W_0^2}\right)^2\right], \qquad R(z) = z\left[1+\left(\frac{\pi W_0^2}{\lambda z}\right)^2\right], \qquad \phi_n(W,R) = \left(n+\frac{1}{2}\right)\arctan\left(\frac{\pi W^2}{\lambda R}\right). \tag{6}$$

Thus, any object at $z=0$ can be projected into a truncated basis defined by a maximum order M and an initial waist W_0, and one can compute continuously the propagated field at any distance z. There exist numerous ways to choose M and W_0 [19], a good trade-off between the spatial extent of the object T and its resolution ΔX is to take:

$$W_0 = \sqrt{\frac{T\Delta X}{2\pi}}, \qquad\qquad M = \left\lfloor\left(\frac{T}{2W_0}\right)^2\right\rfloor \tag{7}$$

where $\lfloor\cdot\rfloor$ denotes the integer floor rounding.

2.2.2 Atmospheric refraction

The most important effect occurring when oblique starlight travels into the atmosphere is lateral refraction, that shifts the actual shadow by 3 m (for 45 deg zenith angle at λ=0.5 μm) from the position it should have in vacuum [9]. But since the star and the satellite are identically affected, refraction has no impact on the shadow shape and should only be marginally taken into account as usual when positioning the telescopes.

More important is the chromatic variation of this shift, that reaches 26 cm/μm in the visible band [9]. This contrast loss has to be considered on wide spectral channels (several hundred nanometers) [10]. But when measurements are made on narrow spectral bands (of a few tens of nanometers, as imposed by diffraction), the intraband chromatic shift is only a few centimeters and proves to be of little consequence as long as each channel shift is numerically accounted for in the multi-band processing.

2.2.3 Atmospheric turbulence

Another important effect of atmosphere on high-resolution systems is turbulence. It is trivial to show that phase errors, that critically limit the performance of telescopes and interferometers, are identically seen by the shadow and the local oscillator and thus are discarded by the quadratic detection.

However, the propagation from the highest atmospheric layers generates intensity variations over the pupil known as scintillation. They are still identical for the shadow and the local oscillator, but will randomly differ over the sub-apertures. Previous numerical simulations have shown that shadow imaging is robust to scintillation [5, 8]. Based on a Kolmogorov turbulence model, we have computed the scintillation filtering induced by the spatial averaging over the telescope pupil and the temporal freezing over a short measurement time [10]. It turns out that the intensity variation due to scintillation are small enough not to hamper the inversion algorithm in usual conditions (absence of fast jet-stream).

2.3 Benefits of the method

Shadow imaging is robust to phase variations because the diffracted field originates from the interference between the plane wave of the star and its part diffracted by the satellite. Since these two waves travel along the same optical path, they undergo the same phase variations and keep a common reference. The phase differences between the telescopes remain, but they have no impact because the light beams are not optically manipulated (the rays collected by each telescope do not interfere with each others), we simply measure the intensity and process the whole set of measurements numerically.

In contrast to conventional methods that rely on the optical combination of coherent light beams collected over one big aperture or several small apertures, in shadow imaging, reconstruction by solving the inverse problem acts as a numerical combination of the light collected by the telescope array, which greatly simplifies the assembly and allows the use of powerful digital tools. And even if the measure is solely done in the pupil plane, the collected intensity contains the modulation of the plane wave by the object and hence provides information about the object's structure. Shadow imaging is in fact a large-scale innovative application of digital in-line holography [20].

3. OBJECT RECONSTRUCTION IN SHADOW IMAGING

3.1 Sampling the diffracted shadow

A key point in sizing a shadow imaging system is to set the number, spacing and diameter of the telescopes. The telescope spacing sets the sampling period of the shadow while the number of telescopes (at a given spacing) sets the support of the acquired shadow. To derive these parameters, we rely on the properties of HG functions, as they offer a quasi finite support.

In particular, when an object is represented by a truncated basis of waist W_0 and maximum order M, the spherical wave in Eq. (5) gives the diffracted field $\overline{U_z}$ a local frequency f_{loc} that varies linearly with the distance from the center x. From Eq. (5), we get that f_{loc} is upper bounded by:

$$f_{\text{loc}}(x) \leq \frac{\sqrt{M}}{\pi W_{\text{GEO}}} + \frac{x}{R_{\text{GEO}}\lambda}, \tag{8}$$

where R_{GEO} and W_{GEO} are given by Eq. (6). Whereas, rather than measuring the diffracted field, the detector measures its intensity defined as:

$$I(x) = |1 - \overline{U_z}(x)|^2 = 1 - 2\text{Re}\left(\overline{U_z}(x)\right) + |\overline{U_z}(x)|^2. \tag{9}$$

Hence, strictly speaking, the sampling frequency in the image plane should at least be 4 times the maximal instantaneous frequency of the diffracted field given by Eq. (8), to account both for the Shannon criterion and the square modulus of the field. Fortunately, the term $2\text{Re}\left(\overline{U_z}\right)$ becomes overriding far from the shadow center. This means that when the extent of the shadow is large enough, one can simply correctly sample the real part of the field while ensuring that the square modulus part as well is properly sampled in the centre of the shadow. In this case, denoting by $x_{\max}$ the largest x-coordinates of the shadow, the maximal frequency of the diffracted field is written:

$$f_{\max} = \frac{\sqrt{M}}{\pi W_{\text{GEO}}} + \frac{x_{\max}}{R_{\text{GEO}}\lambda_0}, \tag{10}$$

computed at the central wavelength λ_0 for convenience, which gives a sampling period of:

$$\Delta x = \frac{1}{2f_{\max}}. \tag{11}$$

Next, we need to estimate the spatial extent of interest of the shadow, given by $x_{\max}$. One way to do that is to use the nearly finite support of HG functions, expressing $x_{\max}$ according to the waist W_{GEO} in the detector plane and M the higher order, such that:

$$x_{\max} \approx W_{\text{GEO}}\sqrt{M}. \tag{12}$$

However, this $x_{\max}$ is given for noiseless measurements in an infinitely narrow observation bandwidth. Indeed, one of the factors limiting the resolution on the object are the spectral and spatial coherences of the light source, which will progressively attenuate the diffraction rings, making the most extended HG function (spatially and therefore frequency-wise) difficult to detect. We assume here that the light source is point-like, and in order to ensure that the rings in the edge of the diffractogram are not blurred by the spectral extension of the source, its coherence length must be larger than the optical path difference between the two points of the spherical wave and the plane wave that are combined at the edge of the shadow. Hence, the spectral width $\Delta\sigma = \Delta\lambda/\lambda_0^2$ of a detection channel must satisfy the condition [21]:

$$x_{\max} \leq \frac{T}{2} + \frac{1}{\Delta\sigma^2}\sqrt{1 + 2z_{\text{GEO}}\Delta\sigma}. \tag{13}$$

Knowing $x_{\max}$ and looking for $\Delta\sigma$, Eq. (13) is approximately equivalent to:

$$\Delta\sigma \leq \frac{2z_{\text{GEO}}}{(x_{\max} - T/2)^2}. \tag{14}$$

Another important limiting effect is caused by the various noise sources, mainly the shot noise, sensor quantification noise, dark current and stellar background. These parameters, coupled with a chosen SNR level, will set a high limit for the magnitude of the occulted star.

3.2 Inversion algorithm: maximum *a posteriori*

The phase of the diffracted field is only partially lost during the measurement of the intensity as we can see in Eq. (9) that it is still encoded in the real part of the field. In order to recover the whole phase that corresponds to the measured intensity, a phase retrieval algorithm must be used. The earliest such algorithm for Fraunhofer diffraction is a back-propagation method by Gerchberg and Saxton [22]. For satellite shadow imaging, Douglas [23] employed his version adapted to Fresnel diffraction. Although these projection methods are intuitive and provide rather satisfactory results, they have some disadvantages. For example, twin image artifacts may appear, noise statistics and the quality of the measurement points cannot be taken into account and only strict constraints on the object of interest can be applied. An approach to overcome these limitations is to use modern optimization methods, where an objective function to be minimized is explicitly stated.

In order to benefit from the polychromatism of the source without inducing losses of contrast due to the chromatism of diffraction and atmospheric refraction, we define a polychromatic objective function J that is the weighted sum of several terms J^{λ_i} each taken on a narrow spectral band at a wavelength λ_i, such that:

$$J(\alpha) = \sum_i \beta_i J^{\lambda_i}(\alpha), \tag{15}$$

where the β_i are real positive coefficients which includes the discrepancies between the intensities at different wavelengths, due for example to the absorption of the atmosphere or the quantum efficiency of the detector, and

$$J^{\lambda_i}(\alpha) = A^{\lambda_i}(\alpha) + \nu R(\alpha). \tag{16}$$

The objective function to be minimized is expressed as a function of an array of coefficients $\alpha = (\alpha_n)_{0\leq n\leq M^2}$ which represent the projection of the object in the chosen HG base. Each A^{λ_i} measures the error between the model and the measured data, $R(\alpha)$ is a regularisation term that adds a prior information on the object, and ν is an hyperparameter that allows to change the relative weights between the two terms. A^{λ_i} is given by:

$$A^{\lambda_i}(\alpha) = \|I^{\lambda_i}_{\text{mes}} - I^{\lambda_i}_{\text{calc}}(\alpha)\|_2^2, \tag{17}$$

where $\|\cdot\|_2$ is the L^2 norm on the 2D measurement grid that can include the discrepancies between the measurement points. The diffracted intensity calculated using the propagation model is written

$$I^{\lambda_i}_{\text{calc}}(\alpha;x,y) = |1 - \overline{U}^{\lambda_i}_{z_{\text{GEO}}}(\alpha;x,y)|^2 \quad \text{for all } (x,y) \in [-x_{\max}, x_{\max}]^2. \tag{18}$$

with $\overline{U}^{\lambda_i}_{z_{\text{GEO}}}$ being computed using the object's coefficients and the 2D HG functions in the detector plane ($\phi_n^{z_{\text{GEO}}}$):

$$\overline{U}^{\lambda_i}_{z_{\text{GEO}}}(\alpha;x,y) = \sum_{n=0}^{M^2} \alpha_n \phi_n^{z_{\text{GEO}},\lambda_i}(x,y) \quad \text{for all } (x,y) \in \mathbb{R}^2. \tag{19}$$

As for the regularization term $R(\alpha)$, we use it to incorporate in a flexible way the *a priori* that the satellite is a completely absorbing opaque object. One very common form of this constraint in phase retrieval methods is the total variation regularization as it favors smooth solutions while preserving sharp edges. It is defined as:

$$R(\alpha) = \sum_{k,l} \sqrt{\|\nabla_{X,Y} S(\alpha, X_k, Y_l)\|^2 + \varepsilon}, \tag{20}$$

where $\nabla_{X,Y}$ is the spatial gradient in the satellite plane and $\varepsilon > 0$ makes the criterion derivable. Like the sought object, the regularisation does not depend on the observation wavelength.

3.3 Polychromatic numerical experiments

We start by evaluating our polychromatic inversion algorithm on simulated data. We choose to study a 15 m × 15 m satellite depicted in Fig. 3a, and we intend to recover details of at least 75 cm. At an altitude of 40 000 km, the diffracted intensity has a Fresnel number of 10 at 550 nm. The intensity supplied to the inversion algorithm was generated by the direct diffraction model, with the addition of a Poisson noise simulating the star's shot noise. According to Eq. (7),

the size of the object and the targeted resolution require an initial waist $W_0 = 1.3\,\mathrm{m}$ and a maximal order $M = 31$, and the latter parameters result in a $2x_{\max} = 60\,\mathrm{m}$ long shadow, well sampled for $\Delta x = 30\,\mathrm{cm}$. Hence, we choose the telescopes' diameter to be 30 cm. To avoid being restricted by the diffraction chromatism, Eq. (14) dictates a maximal spectral bandwidth of 40 nm at 550 nm and we choose a spectral bandwidth of 20 nm.

Fig. 3b shows the coefficients of the object in the HG function basis. This is the array that we are looking for when minimising the optimisation criterion.

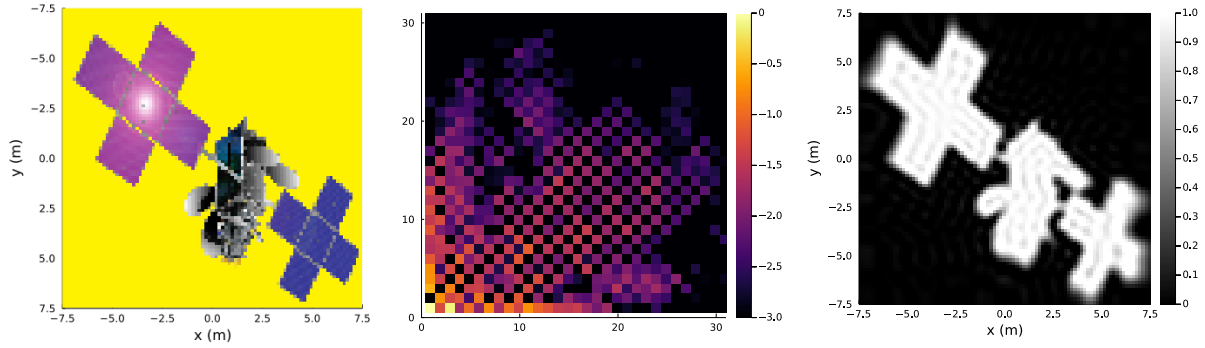

(a) Reflectance of the simulated satellite.

(b) Satellite's coefficients in the HG basis (logarithmic scale).

(c) Projection of the object's HG coefficients in the pixel basis.

Fig. 3: Satellite discretization.

The following subsection aims to study the relevance of the polychromatic inversion. To begin with, we apply the inversion algorithm in one sole spectral channel centered at 550 nm for a star of magnitude 5. This reconstruction will serve as a reference for the multiple spectral channels problem. Fig. 4 shows the diffracted intensity and the retrieved object is displayed in Fig. 5a. Since the object used to generate the measured intensity is known, a relative root mean square error $RMSE_\mathrm{r}$ can be calculated between the sought object and the reconstructed object. We notice in Fig. 5a that the retrieved object matches well the initial one, and that is also reflected in a value of the $RMSE_\mathrm{r}$ of 8.6%. Then, we consider the same reconstruction but performed in parallel on 20 spectral channels from 400 nm to 800 nm, but this time with 20 times less photons received per measurement. More specifically, dividing the number of photons by 20 is equivalent to considering a star with a magnitude 3 points higher. Shadow extent is chosen according to the minimal wavelength. The resulting retrieved satellite is shown in Fig. 5c and has an $RMSE_\mathrm{r}$ of 9.7%. To make this result more meaningful, the single-wavelength case was also inverted for a 20 times smaller number of photons, the reconstructed satellite (in Fig. 5b) shows an $RMSE_\mathrm{r}$ of 26%. Thus, it can be said that measuring at several spectral channels in parallel did, indeed, increase the total SNR and resulted in a significantly better reconstruction. Equally, this gain in SNR means that we can afford to use higher magnitude stars.

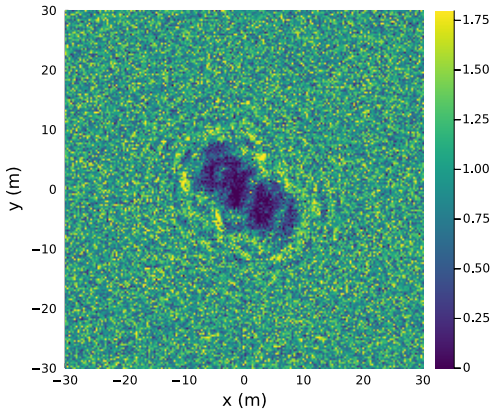

Fig. 4: Diffracted intensity at 550 nm

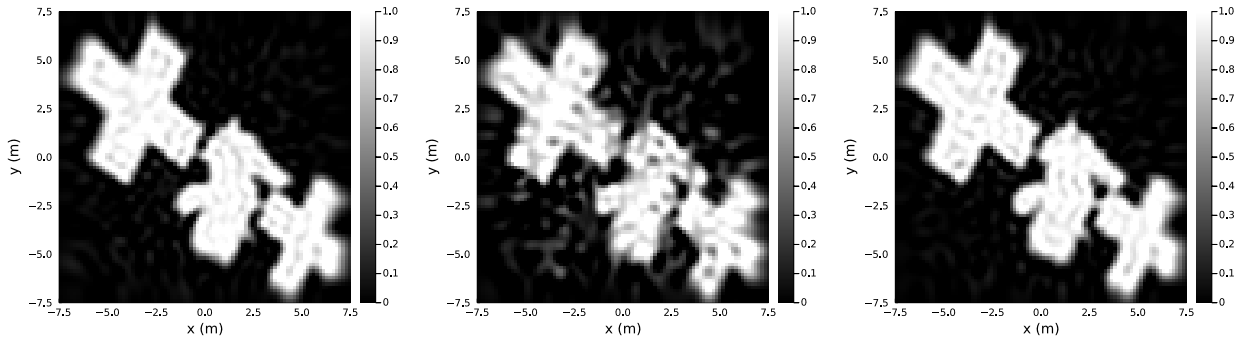

(a) High SNR, single spectral channel reconstruction, $RMSE_r = 8.6\%$.

(b) Low SNR, single spectral channel reconstruction, $RMSE_r = 26\%$.

(c) Low SNR, multiple spectral channels reconstruction, $RMSE_r = 9.7\%$

Fig. 5: Object reconstruction in one and multiple spectral channels.

Sampling according to the Shannon criterion requires several hundred measurement points along the north-south direction. The previous numerical experiment was conducted on well-sampled intensity map, which in the previous case results in a total number of 160 telescopes being required. Yet, under-sampling definitely leads to aliasing issues in the shadow, which may induce a loss of resolution on the reconstructed object. One way to reduce the number of points without compromising the resolution is to compensate for the lack of information due to undersampling by observing on several different spectral channels. In fact, the diffracted field, between two neighbouring narrow spectral channels, is essentially homothetic. Measuring the intensity at a single point but at several spectral channels is therefore almost equivalent to sampling the same signal at several spatially distributed measurement points. Using multiple wavelengths to improve reconstruction is current practice in digital holography [24, 25]. Moreover, multiplying the wavelengths is analogous to a phase diversity technique, in the sense that the modulation of the plane wave by the object strongly dependents on the wavelength, while the reference plane wave is not wavelength dependent.

To illustrate our intuition, we reproduce the previous inversion for a star of magnitude 5 and on 20 spectral channels in parallel from 400 nm to 800 nm. Shannon criterion implies at least 160 measurement points, and we will reconstruct the object with only 40 points distributed evenly over the shadow plane. Four of the diffracted intensities used are shown in Fig. 6 and we can clearly notice that they are undersampled. The measurements are deliberately spaced out to see the difference between the measurements. Despite this undersampling, the result displayed on Fig. 7 shows a successful reconstruction of the object with an RMSE of 7.9%, i.e. an even better reconstruction than the previous one at 550 nm well sampled at the same SNR.

4. LABORATORY EXPERIMENTS

4.1 Experimental setup

In order to work on real measurements while bypassing the difficulties inherent to on-sky observations, we have constructed an experimental setup to study shadow imaging on a small scale, schematically illustrated in Fig. 8. We were inspired by Paxman's work [7] though we mainly attempt here to explore the polychromaticity of the inversion. Our objective is to represent diffraction for a Fresnel number of 12 at a central wavelength of 550 nm, which corresponds to a 16 m satellite at about 40 000 km from an observatory in metropolitan France. We consider the diffraction for three different spectral channels $\lambda_1 = 500$ nm, $\lambda_2 = 550$ nm and $\lambda_3 = 600$ nm all at $\Delta\lambda = 40$ nm $\pm$ 8 nm. The reference wavelength is 550 nm.

The optical bench is shown in Fig. 9. The light source representing the occulted star is a DC-regulated halogen lamp operating at 3400 K, paired with three narrow band filters and a single-mode optical fibre (P2-460B-PCSMA-1 from THORLABS). The single-mode fibre provides a single Gaussian mode, which emulates a spatially coherent point star. As for the satellite flying in the sky, we replaced it with an object printed by photolithography on a one-inch diameter fused silica flat. In order to avoid defects on the shadow due to small phase variations induced by the plate, we chose a dual surface plate with a high precision surface flatness of $\lambda/20$. The object is illustrated in Fig. 9b, it is 1 mm long and contains details that become increasingly thinner, offering a rich frequency spectrum for assessing the quality of

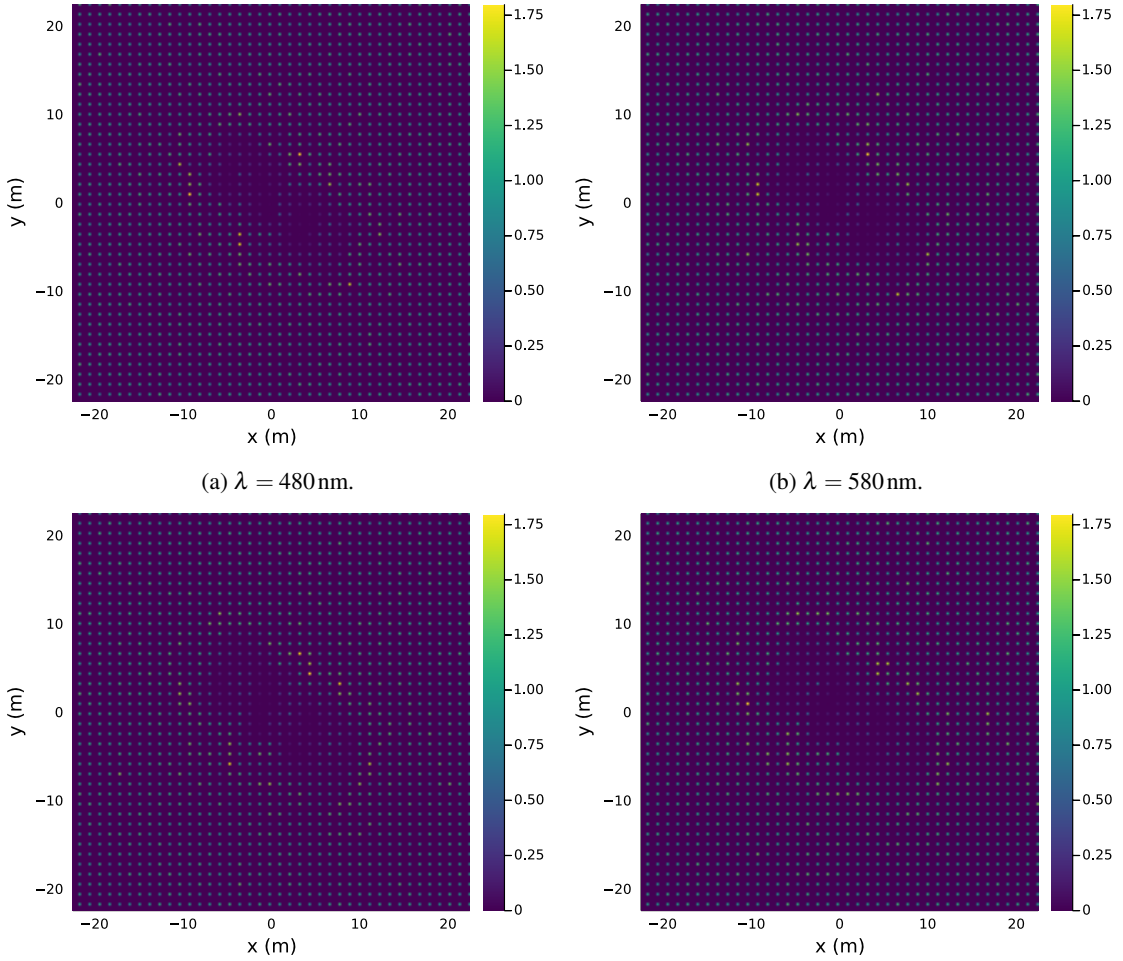

(a) $\lambda = 480\,\text{nm}$.

(b) $\lambda = 580\,\text{nm}$.

(c) $\lambda = 680\,\text{nm}$.

(d) $\lambda = 780\,\text{nm}$.

Fig. 6: Undersampled diffracted intensities.

the reconstruction. And last, as in [7], the ground-based telescopes are simply represented by the pixels of a CMOS camera, here an IDS UI-3060CP Rev. 2, with 1936×1216 pixels of 5.86 µm width. The camera does not have an integrated color filter, so the various acquisitions are made sequentially.

In order to prevent aberrations and wave front errors not initially encountered in shadow imaging, we avoid the use of any collimating lens at the end of the optical fibre. Thus, the LO sent to the camera is a slightly spherical wave and not a plane wave. To compensate for this, the emitted wave will be considered to be plane by performing the linear coordinate change described in [26], that depends on the radius of curvature of the spherical wave. In order to obtain the desired Fresnel number, following the relevant rules given in [26], the object was placed 40 cm from the optical fiber and 24 cm from the camera. The equivalent object-camera distance in plane wave configuration is 39 cm. This also results in a magnification of the object by a factor of $\times 1.6$. To sum-up, in our experiment, everything happens as if an object of 1.6 mm length was illuminated by a plane wave, and located at 39 cm from the camera.

4.2 Reconstructions using one single narrow-band observation

In the 1 mm long object, we aim at recovering details of length Δx = 40 µm, which is equivalent to 64 µm when taking into account the magnification due to the spherical wave. To have some margin with regard to the positioning of the object, we consider a support 2.2 mm long. Under these conditions, Eq. (7) gives a waist W_0 of 149 µm and a maximum order $M = 53$. Then, using Eq. (10) we get a maximal spatial frequency of $f_{\max} = 19.6\,\text{mm}^{-1}$, requiring a distance between the measurement points of at least 4.36 pixels, equivalent to a distance of about 26 cm in real scale conditions. This distance sets the spacing between the telescopes (the measurement points) and provides an upper

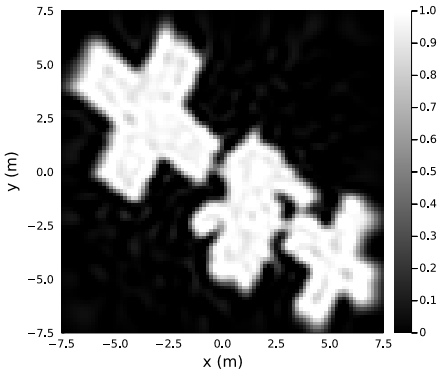

Fig. 7: Satellite reconstruction using undersampled intensities and multispectral inversion.

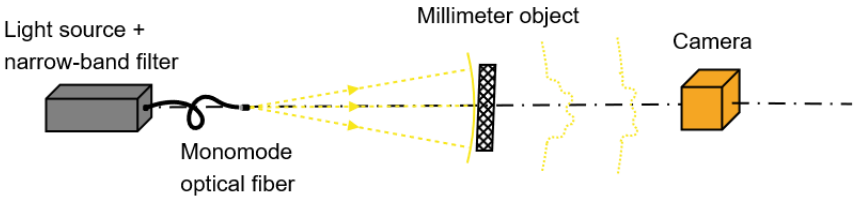

Fig. 8: Schematic of the optical bench.

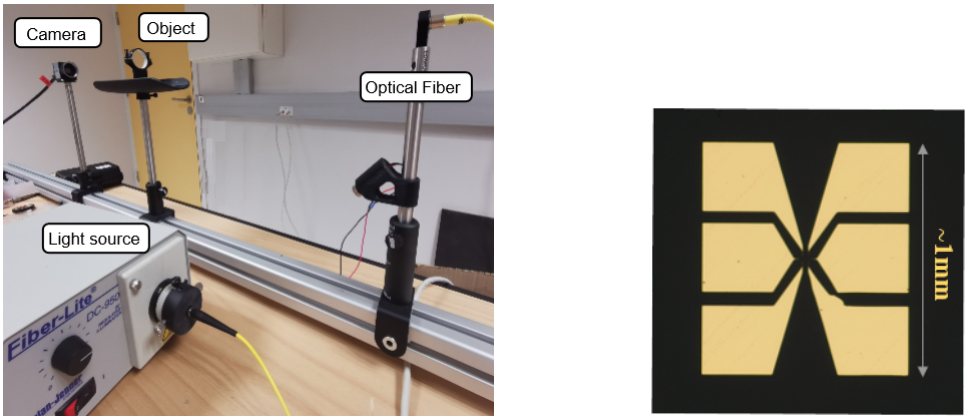

Fig. 9: The optical bench: overall view (a, left) and detail of the object (b, right).

bound for the telescope diameter (the width of the light collector). Eq. (12) allows us to calculate the effective half extent of the shadow $x_{\max} = 3.4\,\text{mm}$. Reconstructions are therefore carried out on a square of 1216×1216 pixels, we take a little margin because the shadow is not perfectly centred on the image. To simulate the observation by telescopes of about 25 cm diameter, we concatenate for each single measurement the intensities collected by 4×4 pixels. This is not absolutely necessary here because the SNR is very good, but in real scale shadow imaging, it will allow us to increase the number of collected photons and improve the SNR. Binning the shadow here also enables us to experimentally simulate the averaging effect due to the telescope's aperture. The full frame diffractograms obtained from measurements at the three different wavelengths are shown in Fig. 10. Few defects can be noticed on the three intensity maps, they are due to dust present on the flat plane at the time of acquisition.

Measurements at the three wavelengths are made for the reference values at 550 nm, so the intensity is a bit undersampled at 500 nm and oversampled at 600 nm. When no object is included and 4 pixels are concatenated per measurement, the SNR is 28 at λ_1, 31 at λ_2 and 43 at λ_3. The disparities are caused by the quantum efficiency of the camera sensor and the spectral radiance of the light source.

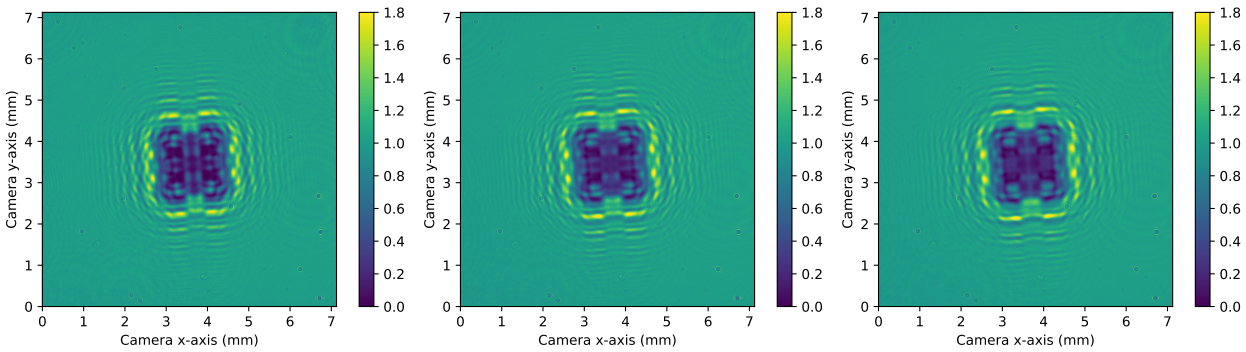

(a) $\lambda_1 = 500\,\text{nm}$. (b) $\lambda_2 = 550\,\text{nm}$. (c) $\lambda_3 = 600\,\text{nm}$.

Fig. 10: Normalized diffracted intensity maps for the three wavelengths.

We begin by applying the reconstruction algorithm to the 4×4 binned intensities. All reconstructions have been made with a stopping criterion being an absolution deviation between successive estimated coefficients of less than 10^{-6}, with regularisation factors $\nu = 10^{-6}$ and $\varepsilon = 10^{-2}$. Moreover, the algorithm behaves in the same way for all measurement points. Fig. 11 shows the obtained reconstructions for each spectral channel. In order to truly compare and evaluate the three reconstructions, the intensity values for a column shown in red in Fig. 12a, and for the three spectral channels are plotted in Fig. 12b. Furthermore, with the aim of comparing the width of the large arm of the object (the smoothed rectangular function visible three times in Fig. 12b) with its real value ($\approx 1.6 \times 290$ µm), the HG coefficients found each time were projected into a finer mesh, and each retrieved object was numerically rotated so that it is parallel to the vertical axis.

At first sight, the reconstructions are very satisfactory, the general dimensions of the object are respected and fine details of the object are restored, the targeted 64 µm resolution is also largely recovered. In particular, the defect at the bottom right of the object (Fig. 9b) seems to be very well rendered despite being smaller than the targeted resolution. And if we take a close look at the cross-section in Fig. 12b, we can see that the reconstruction at λ_3 is a little better than the other two spectral channels, this is probably due to the higher SNR. As for the arm size, we find a full width at half maximum of 469 µm which is very close to the real value of approximately 467 µm.

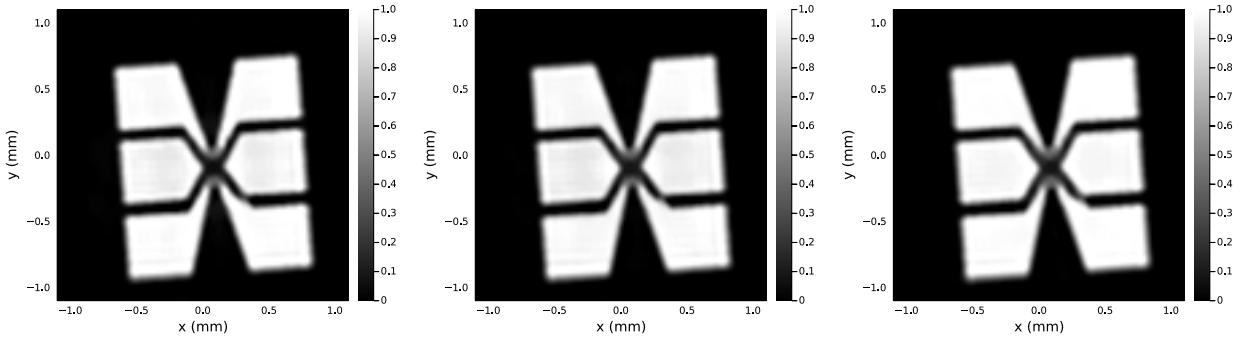

(a) $\lambda_1 = 500\,\text{nm}$. (b) $\lambda_2 = 550\,\text{nm}$. (c) $\lambda_3 = 600\,\text{nm}$.

Fig. 11: Solution of the inverse problem at each spectral channel.

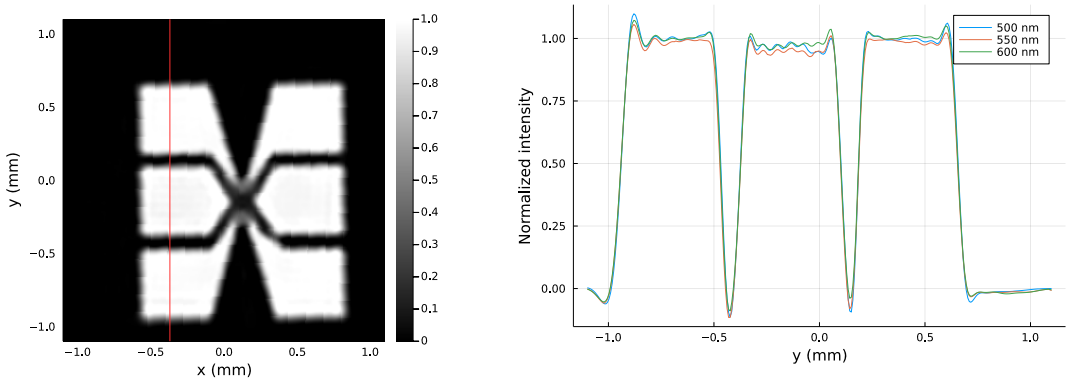

(a) Rotated object.

(b) Value of the reconstructed object on the indicated red cross section.

Fig. 12: Cross section view of the object.

4.3 Reconstructions using multiple narrow-band observations

The main advantage of making several measurements at different wavelengths at each point is to increase the SNR by collecting a larger number of photons. To visualise this SNR gain and its impact on the reconstruction using the experimental set-up, we place the acquisition in a less favourable case than the previous one. Specifically, the exposure time of the camera is reduced so as to decrease the SNR by reducing the received flux, to achieve an SNR between 6 and 7 for the three wavelengths. The SNR at λ_2 is equivalent to a star of magnitude 6.3. Fig. 13 shows the three low-SNR full-frame intensities. A 4×4 binning is applied to these intensities, and then the inversion algorithm is run on each spectral channel separately, with exactly the same parameters as used before. Results are shown in Fig. 14. We first notice that, despite the noise, the three reconstructions have converged well towards the desired object. However, the centre of the object is much less resolved than in Fig. 11, the noiseless case. Also, we visually notice inhomogeneities inside the object's arms and on the straight edges, especially at 500 nm. This is probably due to the fact that the SNR is a bit lower there, and that the intensity is slightly undersampled there.

Now, let us look at the result of the inversion in Fig. 15a, when combining all the wavelengths together using the objective function defined by Eq. (15). We notice that the sharp edges are much less jagged, the centre is better resolved and there is less variation in amplitude. To observe the gain more accurately, the amplitude on a cross section of the object is plotted for the four reconstructions in Fig. 15b. However, the gain is much less visible than in the numerical experiments, we believe this is due to the sparsity of the spectral channels used, allowed by our experimental setup.

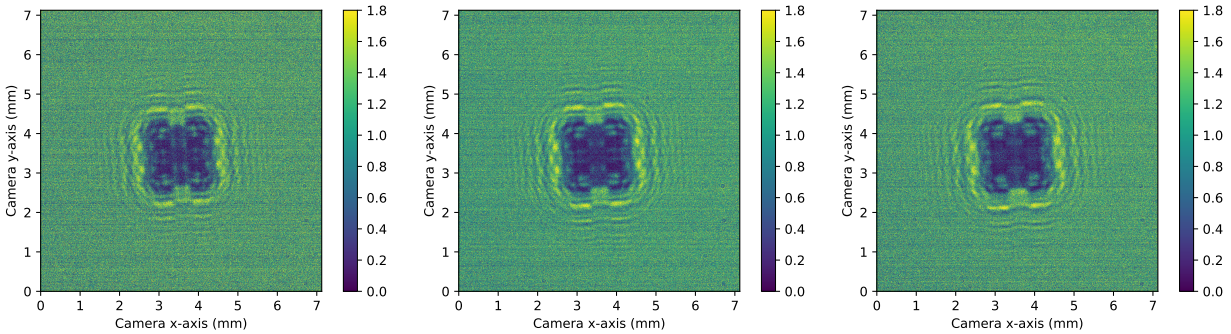

(a) $\lambda_1, SNR = 6.3$. (b) $\lambda_2, SNR = 6.5$. (c) $\lambda_3, SNR = 7.5$.

Fig. 13: Diffracted intensities for low SNRs at the three wavelengths.

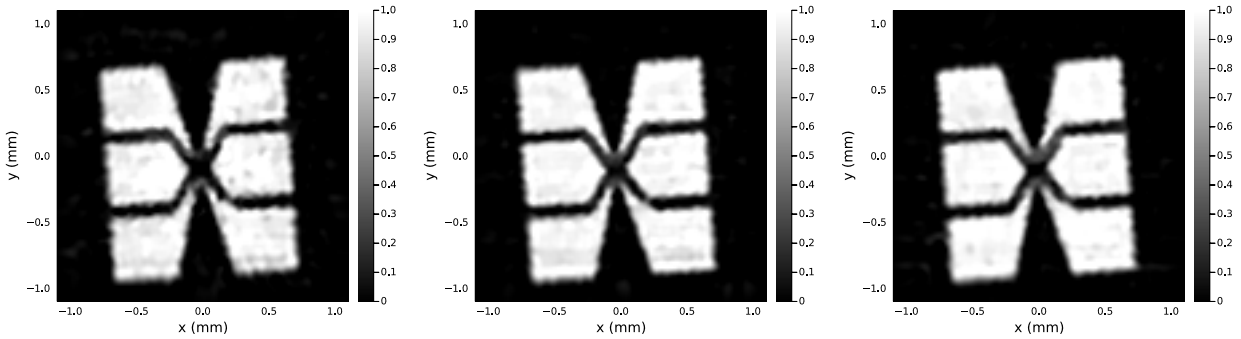

(a) $\lambda_1, SNR = 6.3$. (b) $\lambda_2, SNR = 6.5$. (c) $\lambda_3, SNR = 7.5$.

Fig. 14: Solution of the inverse problem for low SNRs at the three wavelengths.

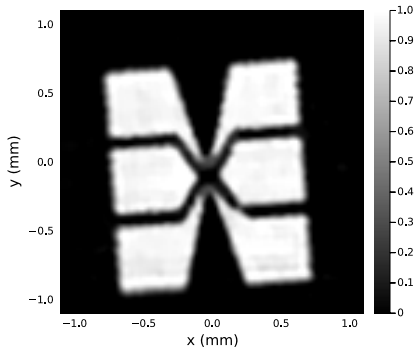

(a) Polychromatic inversion at low SNR.

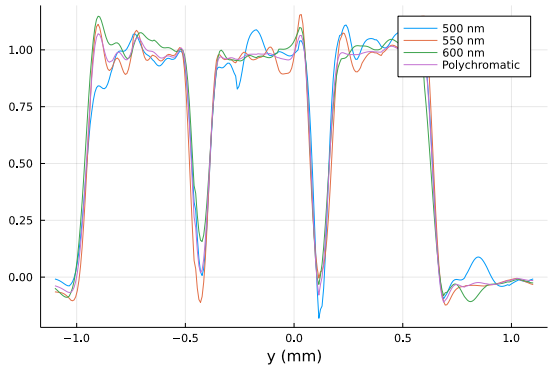

(b) Value of the reconstructed object on the cross section.

Fig. 15: Cross section view of the object.

5. CONCLUSION

This work dealt with the optical propagation of light for shadow imaging of geosynchronous satellites. Shadow imaging is a powerful high-resolution technique to image occulting objects that relies on the much simpler digital combination of the sampled intensities rather than the coherent optical beams. Shadow imaging is thus intrinsically immune to phase disturbances. As for amplitude disturbances, its extended analytical study agrees with the literature

suggesting that scintillation does not strongly constrain the method. The last atmospheric effect to be taken into account is atmospheric refraction, its effect is not limiting unless the observation is made on one wide spectral channel or several distant narrow spectral bands.

Moreover, Fresnel diffraction has been studied using Hermite-Gauss functions, an orthonormal basis that propagates analytically according to the paraxial wave equation. This modelling allows a physical interpretation of the diffraction parameters, and makes it easier to calculate the support and sampling parameters of the diffracted intensity. Using the propagation model, a polychromatic inversion algorithm based on a *maximum a posteriori* estimator was built.

For the purposes of evaluating the inversion algorithm, several numerical experiments were conducted, assessing the relevance of the polychromatic inversion both to increase the SNR and to relax the sampling constraints. An experimental device close to the real conditions was also designed with the aim of avoiding chromatic aberrations and wavefront errors while making the most of lens-less imaging. Using data acquired under realistic SNR conditions (matching a star of apparent magnitude 6), the retrieved objects reach the expected resolutions which enable the identification of sub-metric details of the object.

All these results comfort us in the interest of shadow imaging for the characterization of geostationnary satellites.

ACKNOWLEDGMENTS

The authors thank Anthelme Bernard-Brunel for his contribution to the laboratory setup and Paul Chapelier, Claude Chartier and Raphaël Geng from Onera/DPHY for the manufacturing of the sample object by photolithography. The work of all authors has been funded by Direction Scientifique Générale of ONERA in the framework of the Costello project. The PhD work of H. Labriji is co-funded by Paris-Saclay University.

6. REFERENCES

[1] J. Drummond and R. Rast. *First Resolved Images of a Spacecraft in Geostationary Orbit with the Keck-II 10 m Telescope*. In S. Ryan, editor, *Advanced Maui Optical and Space Surveillance Technologies Conference*, page E21, September 2010.

[2] H Schmitt, JT Armstrong, EK Baines, SR Restaino, JH Clark III, JA Benson, DJ Hutter, and RT Zavala. *Multiple-baseline detection of a geostationary satellite with the Navy Precision Optical Interferometer*. In *Advanced Maui Optical and Space Surveillance Technologies Conference*, volume 8, 2015.

[3] F Roques, M Moncuquet, and B Sicardy. *Stellar occultations by small bodies-Diffraction effects*. *The Astronomical Journal*, 93:1549–1558, 1987.

[4] R. H. Burns, V. Gamiz, J. J. Dolne, J. Lambert, and S. Long. *Shadow imaging of GEO satellites*. In *Unconventional Imaging*, volume 5896, page 58960C. International Society for Optics and Photonics, August 2005.

[5] D. M. Douglas. *Shadow imaging of geosynchronous satellites*. Thèse de doctorat, Arizona State University, 2014. ISSN: 9781321180817.

[6] R. Paxman. *Synthetic-Aperture Silhouette Imaging (SASI)*. In Sandy Ryan, editor, *Advanced Maui Optical and Space Surveillance Technologies Conference*, page 103, September 2016.

[7] R. G. Paxman, K. W. Gleichman, A. S. Iacchetta, and B. M. Jost. *Synthetic-Aperture Silhouette Imaging (SASI) Laboratory Demonstration*. In *Imaging and Applied Optics Congress (2020), paper CTh4C.6*, page CTh4C.6. Optica Publishing Group, June 2020.

[8] J. Luu, L. Jiang, and B. Willard. *Shadow imaging efforts at MIT Lincoln Laboratory*. In *Advanced Maui Optical and Space Surveillance Technologies Conference*, page E34, 2008.

[9] H. Labriji, O. Herscovici-Schiller, and F. Cassaing. *Computation of the lateral shift due to atmospheric refraction (Forthcoming). Astron. Astrophys.*, 2022.

[10] H. Labriji, O. Herscovici-Schiller, and F. Cassaing. *Shadow Imaging of Geostationary Satellites: silhouette reconstruction from accurate polychromatic modelling of diffraction and atmospheric disturbances*. In *9th European Conference for Aerronautics and Aerospace Sciences (EUCASS)*, 2022.

[11] J.W. Goodman. *Introduction to Fourier Optics*. W. H. Freeman, 2017.

[12] C. Aime, É. Aristidi, and Y. Rabbia. *The Fresnel Diffraction: A Story of Light and Darkness*. *EAS Publications Series*, 59:37–58, 2013.

[13] Kyoji Matsushima and Tomoyoshi Shimobaba. *Band-Limited Angular Spectrum Method for Numerical Simulation of Free-Space Propagation in Far and Near Fields*. *Opt. Express, OE*, 17(22):19662–19673, October 2009. Publisher: Optica Publishing Group.

[14] Damien P. Kelly. *Numerical calculation of the Fresnel transform*. *J. Opt. Soc. Am. A, JOSAA*, 31(4):755–764, April 2014. Publisher: Optical Society of America.

[15] Adrian Stern and Bahram Javidi. *Analysis of practical sampling and reconstruction from Fresnel fields*. *OE*, 43(1):239–250, January 2004. Publisher: SPIE.

[16] Gaurav Dwivedi, Sanjit K. Debnath, Bhargab Das, and Raj Kumar. *Revisit to comparison of numerical reconstruction of digital holograms using angular spectrum method and Fresnel diffraction method*. *J Opt*, 49(1):118–126, March 2020.

[17] H. Kogelnik and T. Li. *Laser Beams and Resonators*. *Appl. Opt., AO*, 5(10):1550–1567, October 1966. Publisher: Optical Society of America.

[18] J A Murphy and A Egan. *Examples of Fresnel diffraction using Gaussian modes*. *Eur. J. Phys.*, 14(3):121–127, May 1993.

[19] R. Borghi, F. Gori, and M. Santarsiero. *Optimization of Laguerre-Gauss truncated series*. *Optics Communications*, 125(4):197–203, April 1996.

[20] Bahram Javidi, Artur Carnicer, Arun Anand, George Barbastathis, George Barbastathis, Wen Chen, Pietro Ferraro, J. W. Goodman, Ryoichi Horisaki, Kedar Khare, Malgorzata Kujawinska, Rainer A. Leitgeb, Pierre Marquet, Takanori Nomura, Aydogan Ozcan, YongKeun Park, YongKeun Park, Giancarlo Pedrini, Pascal Picart, Joseph Rosen, Genaro Saavedra, Natan T. Shaked, Adrian Stern, Enrique Tajahuerce, Lei Tian, Gordon Wetzstein, and Masahiro Yamaguchi. *Roadmap on digital holography [Invited]*. *Opt. Express, OE*, 29(22):35078–35118, October 2021. Publisher: Optical Society of America.

[21] F. Soulez. *Gauging diffraction patterns: field of view and bandwidth estimation in lensless holography*. *Appl. Opt.*, 60(10):B38, April 2021.

[22] R. Gerchberg. *A practical algorithm for the determination of phase from image and diffraction plane pictures*. *undefined*, 1972.

[23] D. M. Douglas, B. R. Hunt, and D. Sheppard. *Resolution limits for shadow imaging of geosynchronous satellites: analytic and simulated approaches*. In Jean J. Dolne and Rick P. Millane, editors, *Unconventional and Indirect Imaging, Image Reconstruction, and Wavefront Sensing 2017*, page 24, San Diego, United States, September 2017. SPIE.

[24] Martín Sanz, José Angel Picazo-Bueno, Javier García, and Vicente Micó. *Improved quantitative phase imaging in lensless microscopy by single-shot multi-wavelength illumination using a fast convergence algorithm*. *Opt. Express, OE*, 23(16):21352–21365, August 2015. Publisher: Optica Publishing Group.

[25] Junwei Min, Baoli Yao, Meiling Zhou, Rongli Guo, Ming Lei, Yanlong Yang, Dan Dan, Shaohui Yan, and Tong Peng. *Phase retrieval without unwrapping by single-shot dual-wavelength digital holography*. *J. Opt.*, 16(12):125409, November 2014. Publisher: IOP Publishing.

[26] Edward A. Sziklas and A. E. Siegman. *Mode calculations in unstable resonators with flowing saturable gain. 2: Fast Fourier transform method*. *Appl. Opt.*, 14(8):1874–1889, Aug 1975.